Article | Received 1 May 2024; 21 June 2024; Published 1 July 2024
https://doi.org/10.55092/bm20240005

Micromechanics of osteopontin-deficient bone

Nouf Aldegaither[1,2,3], Xiangli Zhong[4], Eduardo Saiz[1], Sandra J. Shefelbine[5], Alexandra E. Porter[1,*] and Finn Giuliani[1,*]

[1] Department of Materials, Faculty of Engineering, Imperial College London, Prince Consort Road, London, UK
[2] College of Science and Health Professions, King Saud bin Abdulaziz University for Health Sciences, Riyadh, Saudi Arabia
[3] King Abdullah International Medical Research Center, Riyadh, Saudi Arabia
[4] School of Materials, University of Manchester, UK
[5] Department of Mechanical and Industrial Engineering and Department of Bioengineering, Northeastern University, Boston, MA, USA

* Correspondence authors: Alexandra E. Porter and Finn Giuliani;
E-mails: a.porter@imperial.ac.uk; f.giuliani@imperial.ac.uk.

Abstract: Ageing- or bone-related diseases, such as osteoporosis leads to perturbations in the collagenous framework and mineralization that translate to deteriorated fracture resistance at the whole-bone level. However, bulk mechanical testing is insufficient to isolate the effect of these alterations on the mechanical response at a smaller length scale where molecular modifications manifest. Here, we combine *in situ* micromechanical testing using micropillars to determine elastic moduli, double cantilever beam mechanical tests to measure fracture toughness, and transmission electron microscopy (TEM) relate crack propagation at the microscale to local variations in collagen fibril organization. An osteopontin (OPN) knock out bone model with nanometer scale with regions of organised and disorganised collagen matrix and deteriorated fracture resistance at the whole-bone level was used to explore whether it is possible to propagate a crack in a transversely orientated pillar if the collagen fibrils in the pillar are disorganized. The average measured fracture energy for OPN-deficient mouse bone at this length scale, in the transverse direction was 0.94 ± 0.67 J/m^2. This value is significantly lower than wild type bone, which we found in previous studies to be approximately 20 J/m^2. TEM of cross-sections of the cracked pillars showed that the lack of OPN caused disorganization of the fibrillar network, possibly leading to deteriorated fracture resistance in bones. These preliminary findings indicate that OPN may contribute to bone's fracture resistance through collagen matrix organization. This study serves as a starting point for more in-depth investigations that use *in situ* micromechanical testing using micropillars to study interplay between the ultrastructure and fracture resistance in pathologic bone.

Keywords: osteopontin; non-collagenous proteins; bone; fracture energy; toughness; collagen; double cantilever beam

1. Introduction

Ageing- or bone-related diseases, such as osteoporosis are associated with deterioration of skeletal structure, leading to a high risk of fracture [1]. The clinical standard for predicting fracture risk in individuals depends on mineral quantity, which is assessed by measuring bone mineral density (BMD) [2]. However, fracture still occurs in individuals with apparently low-risk BMD [3,4]. Thus, the degradation of bone tissue and its ability to resist fracture cannot be attributed solely to deterioration in the quantity of the mineral matrix. It is crucial that the changes within the organic matrix are also taken into consideration to better elucidate the determinants of impaired bone quality.

Bone's capacity to endure plastic deformation and to resist fracture characterizes bone toughness, which is attributed to toughening mechanisms at different levels of hierarchy such as crack deflection around osteons, micro-cracking, fibrillar sliding, sacrificial molecular bonds, and molecular uncoiling [5]. All of these toughening mechanisms take energy away from propagating the crack thereby increasing bone toughness. We recently examined the fracture energy in in micropillars of normal *murine* bone [6]. The micropillars ($4 \times 6 \times 15$ μm) allowed us to measure fracture toughness in bone tissue below the length scale of osteocyte lacunae, vascular pores, or other features, which could affect crack propagation. In longitudinal pillars, the crack propagated evenly down the length of the pillar. In transverse pillars, the crack immediately deflected to the side, making it impossible to experimentally determine fracture toughness. We estimated the transverse fracture toughness from phase field models that assumed fracture anisotropy in the longitudinal and transverse directions and estimated a transverse fracture toughness double that of the measured longitudinal fracture toughness. This past study clearly demonstrated the influence of fibrillar organization on crack propagation: longitudinal orientation promoted straight cracks and transverse orientation cause crack deflection. In this current study, we explore whether it is possible to propagate a crack in a transversely orientated pillar if the collagen fibrils in the pillar are disorganized. We aim to reveal how closely crack propagation follows the fibril direction. To study this relationship we used bone lacking Osteopontin (OPN), a non-collagenous protein ($OPN^{-/-}$). In our previous work, transmission electron microscopy (TEM) revealed that bones lacking OPN exhibit a highly heterogeneous structure with regions of organised and disorganised matrix, accompanied by spontaneous unwinding of the fibrils in the collagen matrix [7].

The contribution of OPN to bones mechanical properties can be elucidated by using knockout mouse models lacking osteopontin protein ($OPN^{-/-}$). The effect of this OPN mutation on bone mechanisms has been shown to translate through all levels of hierarchy in bone to the whole-bone level [8]. OPN deficiency has been correlated with a decrease in maximum load, work to fracture, post-yield energy dissipation and fracture toughness at the whole-bone level [8–10]. Nanoindentation measurements of elastic modulus indicate that OPN-/- bone has a reduction of modulus of 15% compared to wild type bone [11]. However,

these results do not quantify the contribution of OPN at the length-scale of the mineralised collagen fibrils. There remains a notable scarcity of empirical data relating the local microscale fracture behavior of OPN-deficient bone to alterations in the organization of the fibrilar matrix.

Here we demonstrate OPN-deficient bone is anisotropic by measuring the elastic modulus of micropillars. We then perform a preliminary study of the effects of OPN-deficiency on crack propagation in the transverse direction. We measured the microscale modulus in longitudinal and transverse pillars and the fracture energy in the transverse orientation. We hypothesize that the presence of nanoscale regions of poorly organized tissue, which do not deflect cracks, contribute to reduced transverse fracture toughness in $OPN^{-/-}$ compared to WT bone. Double cantilever beams (DCB) fracture testing was performed *in situ* using a nanoindenter in a scanning electron microscope (SEM) to produce stable crack growth and to generate crack-growth resistance curves (crack length *vs.* fracture toughness) to quantify the fracture properties of $OPN^{-/-}$ bone at the microscale. TEM imaging of cross sections of the fractured pillars was used to image directly fibril organization and structure.

2. Methods

2.1. Bone preparation

Femurs from 8 weeks old $OPN^{-/-}$ knockout mice model (The Jackson Laboratory, USA) were harvested, cleaned of fatty tissue, air dried, and embedded in a low-viscosity resin (Epothin; Buehler, IL, USA) to enable cutting using a low-speed diamond saw (Isomet; Buehler, IL, USA). Animals were obtained with IUCAC approval at Northeastern University. Bones were cured for 48 h at room temperature to avoid using a heat/vacuum chamber for minimal infiltration of the epoxy in the bone tissue.

The embedded femoral diaphysis was cut orthogonally to its long axis at the mid-shaft and then parallel to its long axis to obtain longitudinal sections using the low-speed diamond saw. The sections were then ground and polished with decreasing degrees of diamond slurry from 3 µm to 0.25 µm to flatten the surface; this was followed by subsequent washout of surface impurities. Next, the polished bone section was glued to a SEM stub using a silver conductive paste. A schematic showing the orientation of the longitudinal and transverse pillars for micro-compression and double cantilever beam testing (methods described below in sections 2.2 and 2.3) is shown in Figure S1.

2.2. Elastic modulus measurements

Micropillars were milled from the mid-shaft mid-cortex cross-sections to produce micropillars in the longitudinal (n=6) and transverse (n=5) directions of the bone. Briefly, dual FIB–SEM (FEI Helios NanoLab 600) with a predefined milling pattern implemented in NanoBuilder software was used to fabricate square micropillars with a length of 12–15 µm and a top side length (r_t) of 3 µm (Figure 1a). The aspect ratio (h/r_t) was chosen to inhibit pre-mature buckling and to prevent the pillar's base sinking into the substrate [12–14]. Aspect ratios of

2–4 have been shown to have an insignificant impact on strain measurements [12,15]. Due to the nature of ion milling, achieving a straight pillar can be challenging and lengthy. Most micro-pillars therefore use a taper with the side-length of the pillar's base ($r_{b)}$ larger than the side-length of the top of the pillar. For a tapered pillar, as the angle (θ) increases, the pillar's base cross-section (r_b) increases compared to its top cross-section (r_t), which suppresses the sink-in effect. We used a taper angle $< 5^{\circ}$, which has a negligible effect on strain measurements [12,16] (Figure 1b,c).

A successively decreasing Ga^+ ion current, ranging from 1 nA to 0.1 nA at 30 kV voltage, was followed by a current of 0.1 nA at 5 kV with ± 2° tilted stage to reduce tapering and clean the sidewalls. The FIB machining process of each micropillar took about 7–8 h. From the force/displacement data during compression, we calculated the engineering stress/strain curve. To account for the "sink-in" effect of the pillar sinking into the substrate, we tracked the displacement of a point on the substrate next to the pillar during compression and subtracted this from the total applied displacement to determine the compression of the pillar along. To account for the change in cross-section, we averaged the stress at the top and the bottom of the pillar. From the stress-strain curves we determined elastic modulus, *E*, and ultimate stress. The procedure adapted here was previously reported by Schwiedrzik *et al.* [17].

2.3. Fracture energy measurements

Fracture energy of $OPN^{-/-}$ bone was quantified with DCB micromechanical testing following the protocol outlined in detail in our previous work [6,15]. Micropillars were made (Figure 1a), with a length (l) of 12–15 µm, width (2d) of ~4 µm and thickness (t) of ~6 µm, and a central rectangular trench of ~1.5 µm in width (e) and ~1 µm in height (f) added to its top to produce two shoulders for wedge loading. DCB micropillars were machined in the longitudinal (n=1) and transverse (n=6) directions. Two of the transverse micropillars were excluded from fracture testing, as they exhibited large pores adjacent to the pillar's base. The origin locations of the longitudinal and the transverse micropillars is shown schematically in Figure S2.

The microscale DCB fracture testing was performed *in situ* within a SEM (FEI Quanta 650 FEG-SEM) on the fabricated pillars of OPN-deficient bone using a nanoindenter (Alemnis AG) equipped with a 60° diamond wedge tip. The *in situ* approach offers real-time imaging of tissue undergoing mechanical deformation. The sample was imaged in the SEM in secondary electron mode at 2 kV using at a ~10 mm working distance. The tip's alignment with the pillar's central axis was achieved using a motorised rotary stage in the indenter system. Upon loading the pillar, the displacement of the tip was controlled and quantified using a piezo actuator with a nanometre resolution. By driving down the wedge along the central geometry of the sample, a bending moment to the beams was induced. Under a constant displacement rate of 2 nm s^{-1} of the wedge in displacement mode, the crack initiated and propagated. The crack tip advanced by an increment of length as the strain energy stored in the beams was released. A video was recorded continuously throughout the duration of each experiment.

The *in situ* recorded videos were then processed to register the collected image frames using custom-developed MATLAB (MathWorks, MA, USA) scripts to extract and quantify the beam displacement (δ), beam width (d) and crack length (a). The evaluated outputs were then used to calculate fracture energy (G) based on Timoshenko beam solution [18] to account for the shear deformability of the beams, as follows:

$$G_c = G = -\frac{dU_M}{da} = \frac{3\delta^2 E d^3}{8a^4}\left[1 + (1+\nu)\left(\frac{d}{a¢}\right)^2\right] \quad (1)$$

where U_M is the amount of elastic strain energy stored in each beam per unit depth, ν is Poisson's ratio of cortical bone evaluated as 0.09 for transverse direction [19], a' is the effective crack length considered to capture the rotation deformation at and in front of the crack tip, as Williams's solution proposed [20]. Correction for the root rotation of DCB involves replacing the actual crack length, a, with an effective crack length, a' as ($a + \chi$ d), where χ is a constant that depends on the material elasticity. The value of χ can be determined through numerical solutions and assuming isotropic behaviour, to be approximately 0.67 [20]. Isotropic behaviour was assumed as the values of shear moduli are currently unavailable for mouse cortical bone at this length scale.

The stress-intensity solution for the analysis model of fracture energy applied here was based on linear elastic fracture mechanics (LEFM), which assumes a linear elastic behaviour of the cracked sample [21]. Conforming to LEFM requirements to acquire a valid mode I fracture is generally restricted to the condition of having a sample dimension that is much larger than the size of the plastic zone [21]. To adhere to these requirements, the size of the plastic deformation zone for mode I deformation was estimated to be 2.4×10^{-3} - 7.7×10^{-5} µm, which is three to five orders of magnitude smaller than the sample size (a few micrometres) and in line with the Linear Elastic Fracture Mechanics (LEFM) concept, more details can be found in Figure S3.

For conversion between fracture energy and fracture toughness [21], the following relationship was used:

$$K_I = \sqrt{G\,E¢} \quad (2)$$

where E' is the plane-strain elastic modulus, $E' = E / (1- \nu^2)$, with E determined from the experimental measures of the elastic modulus, $\nu = 0.09$ [19], and G is the fracture energy. Note that the plane-strain elastic modulus was assumed to have an transversely isotropic behaviour rather than the orthotropic equivalent due to lack of data on shear moduli of mouse cortical bone [22].

2.4. Statistical analysis

The propagation of error into the experimental measurements of fracture energy was carried out using a Monte Carlo approach. This adapted analysis method is based on computing the output of a functional relationship—that is, the fracture energy equation—repeatedly, with chosen input variables associated with plausible degrees of uncertainty to produce probability distributions of the targeted outputs. The equation of fracture energy consists of several variables, each of which has an empirically acquired value. Such derived values must also

have associated uncertainties and thus should not be evaluated as constants. Any such uncertainty—associated with systematic and random errors—must also propagate through the functional relationship and contribute to the cumulative uncertainty of the measurement. Therefore, the selected input variables were those that plausibly contributed to the spread in the distribution of the results and were analysed repeatedly. The resulting combined distributions (Figure S4) of each Monte Carlo analysis served as the basis for comparison among all DCBs. Finally, the cumulative mean and standard uncertainties associated with the various output quantities were produced and considered as the respective estimates of each test measurement and standard deviation for each test. Statistical analysis was performed using a custom MATLAB script.

Furthermore, several experimental variables, including geometrical asymmetry effects and the taper angle of the micropillar, were taken into consideration to improve the accuracy of the data analysis; additional details of the experimental approach and analysis can be found in our previous studies [6,15,17].

2.5. Transmission electron microscopy

Site-specific regions in the fractured area of bone were prepared by *in situ* FIB lift out. After mechanical testing, the pillar was returned to the FIB chamber to mill out a TEM foil. A 10 µm platinum layer was deposited on top of the deformed pillar using the electron beam to protect the surface from gallium ion damage, followed by an additional layer of 2 µm of platinum deposited by the ion beam to keep the crack intact. At 30 kV, with a 0.3 nA ion current, two trapezoid trenches around the site of interest were milled, leaving a 2 µm sample. Then a standard lift-out technique was conducted, using a manipulator probe (OmniProbe) to extract and attach the TEM foil onto the TEM grid. Finally, with the cross-section firmly secured to the grid, the thinning process began in successive steps. The thinning progressed at gradually decreasing incidences of the glancing angles (± 3–0.5°), beam currents of (0.1–0.05 nA) at an operating voltage of (16–2 kV). Lastly, due to the fragility of the TEM ultrathin sample (~ 0.15 µm thickness), the final polishing and cleaning was performed with extremely low current (0.02 nA at 2 kV) at ± 7°.

High resolution imaging was carried out using a JEOL 2100 Plus TEM, at an operating voltage of 200 kV. Bright-field images and corresponding selected area diffraction (SAED) patterns of the OPN-fractured tissue were acquired. SAED was performed to obtain the diffraction pattern of the c-axes of hydroxyapatite crystals that coincides with the alignment of the mineralised collagen fibrils. In this way, the orientation of fibrils could be inferred. SAED patterns were obtained using an aperture size of 200 nm and a 0.5 µm spot size. The SAED was indexed to crystalline hydroxyapatite based on JCPDS card no. 9–432.

3. Results

3.1. Elastic modulus

Two distinct modes of deformation were evident in the post-compression images (Figure 1d,e) and the stress-strain curves (Figure 1f,g), indicating strongly anisotropic behavior in the longitudinal and transverse directions. The elastic moduli were more anisotropic than the ultimate stresses (Table 1).

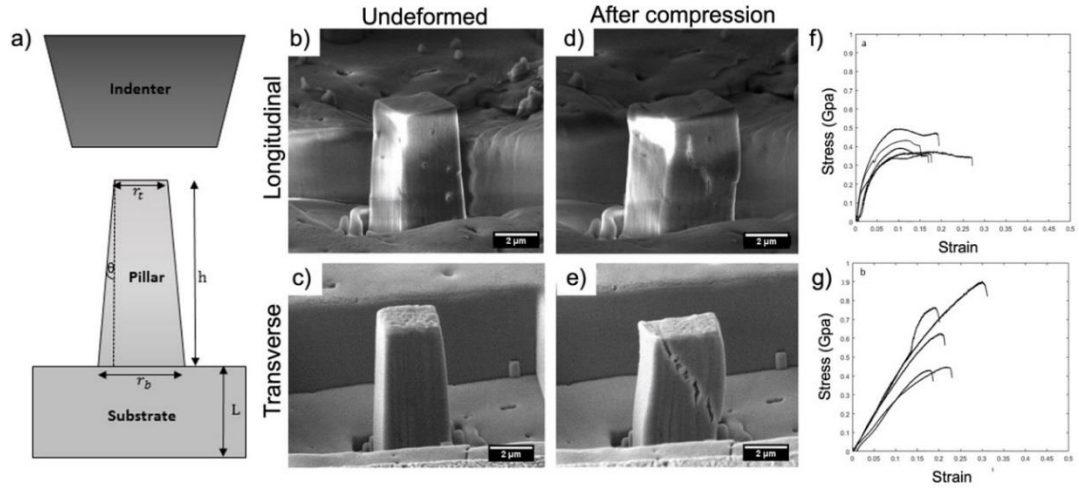

Figure 1. (a) Tapered micropillar dimensions with a top side length $r_t < r_b$ bottom side length. **(b)** longitudinal and **(c)** transverse representative undeformed micropillars. **(d)** Longitudinal and **(e)** transverse micropillars after compression. **(f)** Longitudinal and **(g)** transverse stress strain curves.

Table 1. Elastic properties of OPN-deficient bone.

	Elastic Modulus ± st dv (GPa)	**Ultimate Stress ± st dv (GPa)**
Longitudinal	14.08 ± 4.1	0.4 ± 0.06
Transverse	3.7 ± 0.3	0.6 ± 0.2

When the compression load was applied in the longitudinal direction, the micropillars showed an initial linear elastic response (Figure 2a). At this stage of plasticity, shear bands appeared to form on the outer surface of the micropillar (Figure 2b). After the initiation of shear bands, the localized surface area along the shear slip started to buckle (Figure 2c), and absorbed most of the plastic deformation. Some micropillars lost load-bearing capability and the flow stress subsequently decreased. The relatively unconstrained plastic instability of buckling was preceded by shearing events that initiated kinking and cracks along the fibril direction leading to the final failure (Figure 2d).

When compression was applied to the transverse micropillars, linear elastic behavior (Figure 2e) was followed by a slight deviation from linearity with increasing curvature. This

trend continued to suppress visible deformation (Figure 2f), until a sudden brittle failure at 50°, which was evidenced by the shear processes (Figure 2g). Results suggested that failure here became constrained to the development of a single shear plane with an average angle of 42.4°±7.2° with respect to the compression axis for all micropillars.

Such deformation mechanisms imply that the failure modes were markedly prompted by anisotropy, which introduced axial kinking and cracking when compressed parallel to the main fiber direction (longitudinal). Shear cracking dominated only when the bone was compressed perpendicular to the main fiber direction (transverse).

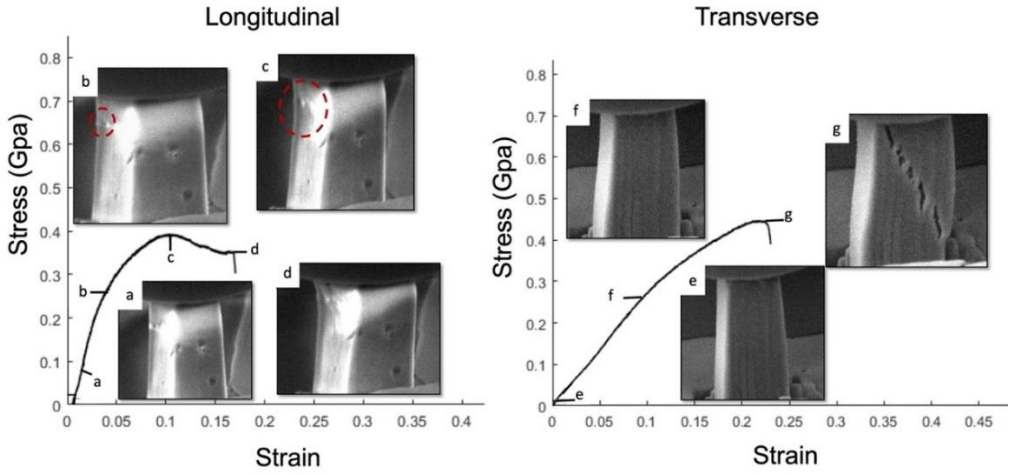

Figure 2. SEM images during the compression of micropillars. In the longitudinal direction, a **(a)** linear elastic region is followed by **(b)** shear bands. Red circles indicate microcracks. **(c)** Buckling of the shear bands occurred at the ultimate stress. **(d)** Shearing initiated longitudinal cracks at failure. In the transverse direction, the **e)** linear elastic region showed **(f)** little visible deformation until **(g)** a shear plane developed at failure.

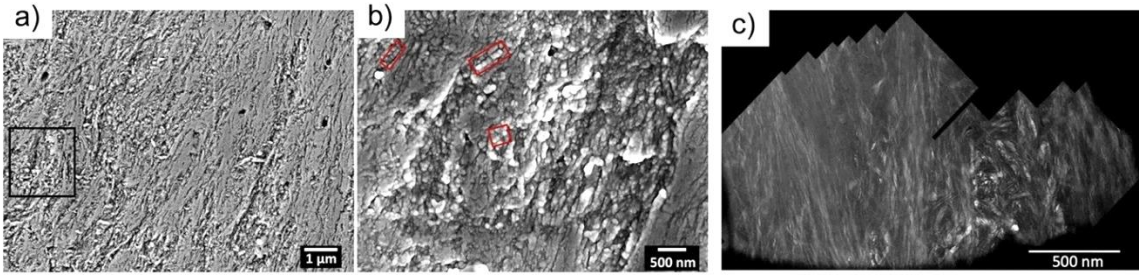

Figure 3. (a) SEM image of the tissue showing localized disarray of fibres. **(b)** The magnified image of the boxed area in (a) displaying fibrils of no apparent order. The red boxed areas show collagen fibrils that display a typical banding pattern, D-periodicity, of about 67 nm as measured in the axial repeating steps. **(c)** TEM image prepared by in situ FIB lift-out showing a localized patch of disorganized fibril adjacent to organized fibrils aligned in the vertical direction. The disorganized patch has no clear banding pattern.

To gain a better insight on the structure of OPN deficient bone, SEM and TEM images were taken on undeformed areas. SEM images revealed fibres disarrayed on both the micro

and nanoscales (Figure 3a,b). TEM images also indicated patchy regions of highly disorganised fibers in the middle of organized fibers (Figure 3c). The micro- to nanoscale structure of the WT healthy bone was significantly more organized (Figure S5).

3.2. Fracture energy

Four transverse pillars were subjected to fracture testing (Figure 4b-e). The fracture behaviour of the bone was categorised into two groups (n=2 in each group). In the first group, a crack propagated straight for approximately 3 µm and then deflected to the edge of the DCB (Figure 4b,c). In the other group, a short straight crack extended; then another immediate and oblique crack appeared, inevitably, to break the DCB shoulder (Figure 4d,e). Only the data from the vertical cracks were used for the fracture energy measurements because the LEFM solution requires a straight crack propagation. Interestingly, although fracture toughness was not assessed from the deviated portion of the crack, the broken surface due to deflection was extremely rough (Figure 4c). Top view examination of the broken shoulder of one of the DCBs by SEM showed an apparent separation of the bone matrix that was bridged by fibrils (red arrows in Figure 4f), suggesting that collagen fibrils can act as bridges across the formed gap.

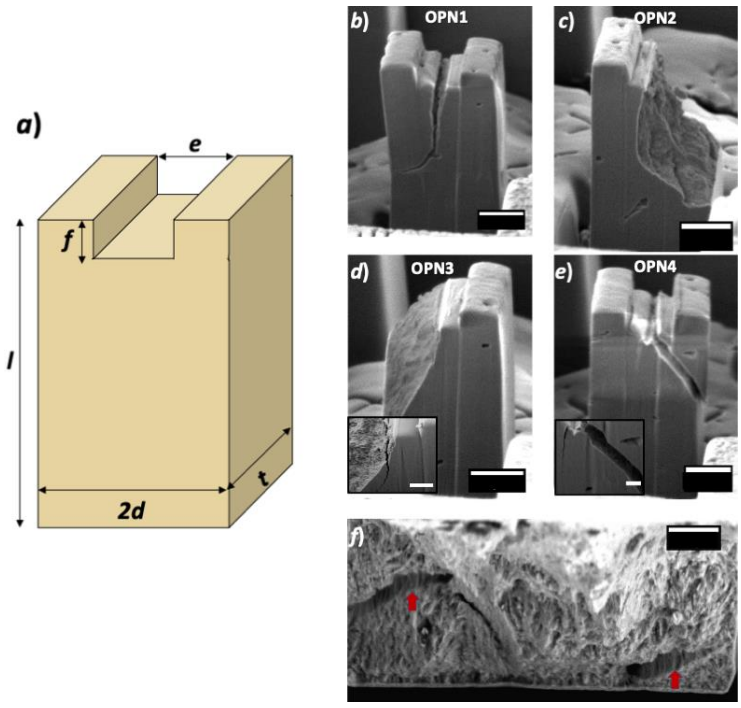

Figure 4. (a) Schematic drawing of the DCB geometry applied in the current experiment. SEM images of OPN−/− DCBs post-fracture tests; **(b,c)** OPN1 and OPN2 displayed a linear straight crack growth before deflecting; **(d,e)** OPN3 and OPN4 show a double crack growth: a straight crack followed by an immediate deviated crack; the former was used for fracture energy measurements . Scale bar: 2 mm (the bottom-left insets show zoomed in view for the fractures, scale bar: 0.5 µm). **(f)** Visual SEM inspection of the top view of the right broken shoulder in (c) revealed a potential detachment of the bone matrix that was bridged by fibrils (denoted by red arrows). Scale bar: 0.5 µm.

The average fracture energy of all OPN$^{-/-}$ samples in the transverse orientation was 0.94 ± 0.67 J/m^2 (Figure 5e,f) as evaluated by Monte Carlo approach. This value is significantly less than that of ~ 26 J/m^2 estimated in our previous work using a phase-field simulation for transverse WT bone (Figure 5e,f) [6].

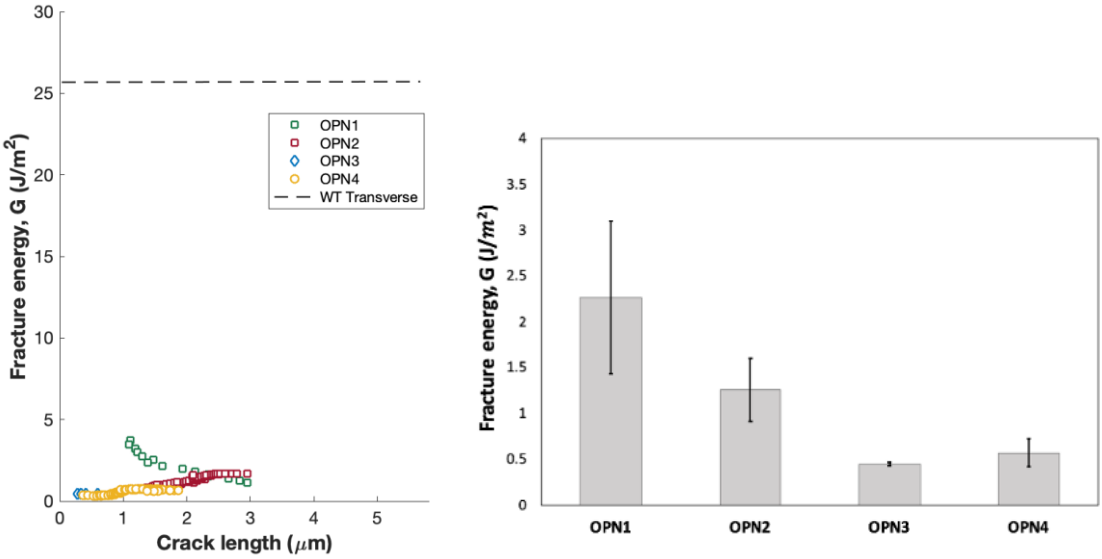

Figure 5. Analysis of microcantilever fracture tests. **(a)** The crack resistance curve shows fracture energy measured as a function of crack length for the bone pillars fractured in the transverse direction. The average fracture energy value measured over crack growth for the four transverse oriented OPN$^{-/-}$ samples is nearly an order of magnitude lower than that reported of WT bone in the transverse direction (indicated by dotted line) [23]. **(b)** the propagation of error into the experimental measurements of fracture energy were carried out using a Monte Carlo error approach. The average value of fracture energy was calculated from only the stable crack-growth region. Ideally this would be > 1µm to reduce error but for OPN3 and OPN4 the crack was only stable over < 1 µm. The error bar represents the standard deviation approximated using Monte Carlo error propagation analysis.

The fibrillar structure of the OPN$^{-/-}$ samples were assessed by bright-field TEM and SAED (Figures 6 and 7) to understand whether the difference in crack path could be related to the altered organisation of the mineralised collagen fibrils. Visualisation of the local nanostructure (Figure 6a) showed the crack path followed by a deflection. In the upper region of the DCB (Figure 6b) and region adjacent to the upper part of the crack (Figure 6c) patches of the collagen fibrils were poorly aligned with no defining orientation. Although, the SAED of this region (using a selected area aperture diameter of 0.5 µm) showed characteristic (002) arcs indicating that the tissue was well aligned (Figure 6d; taken from the region denoted by the upper asterisk in Figure 6a. In contrast, in the region around the deflected crack tip, the collagen fibrils were highly aligned, approximately perpendicular to the DCB's principal axis (Figure 6e). The corresponding SAED pattern of this region (Figure 6g; taken from the area denoted by the lower asterisk in Figure 6a showed a characteristic (002) arc mineralised collagen

aligned perpendicular to the crack axis. A representative region of tissue away from the crack maintained the organised fibrillar assembly, transversely oriented to the crack plane (Figure 6f).

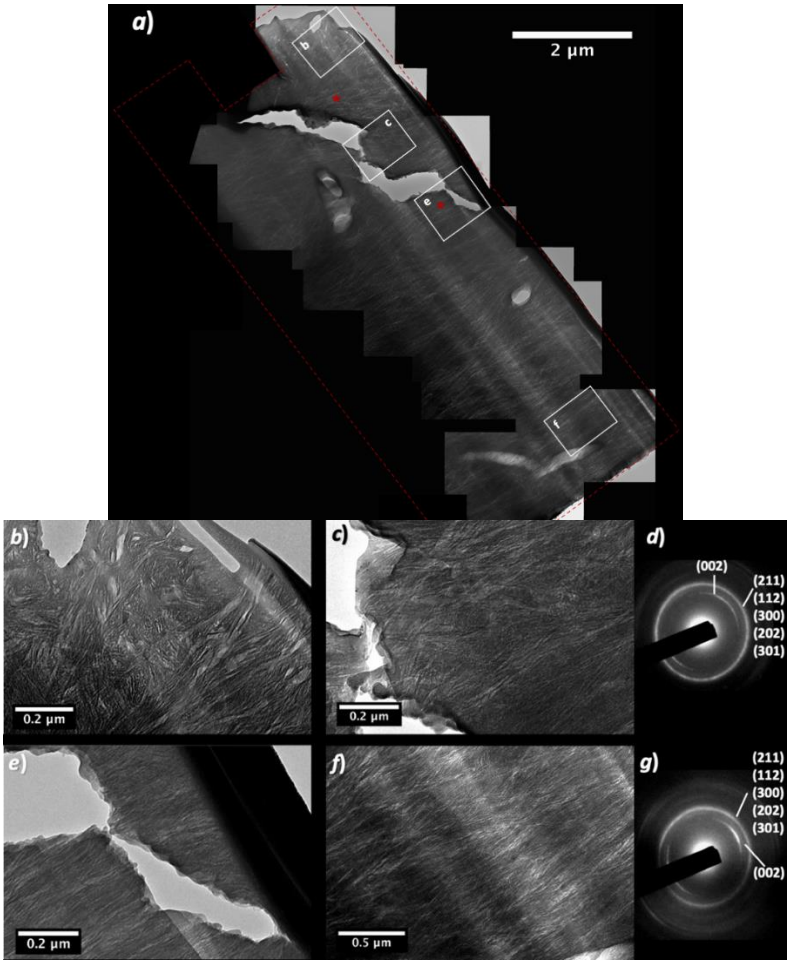

Figure 6. TEM imaging of the fractured DCB of the deficient OPN sample from Figure 4b (OPN1). **(a)** Bright-field TEM image showing the ultrastructure of a cross-section of the sample showing the crack path, the top of the pillar is marked with a red dotted line and it can be seen that there has been some distortion, probably during the sample preparation process. **(b)** The collagen fibrils are made up of regions heterogeneously organized tissue with no clear alignment in the upper [white boxed region b in (a)] and **(c)** middle region of the tissue [white boxed region c in (a)]. **(d)** Corresponding SAED pattern taken from regions indicated by the upper red asterisk in a. **(e)** Before, and around, the deviated crack tip [white boxed region e in (a)] and in the region away from the crack [**(f)**; lower white boxed region f in (a)], the mineralised fibrils align mostly perpendicular to the crack. **(g)** A SAED pattern taken from regions indicated by the lower red asterisk in (a).

Figure 7 shows TEM bright field images and SAED patterns of cross-sections of the fractured OPN-deficient DCB that exhibited double cracking (OPN3 in Figure 4d). Figure 7a shows that the mineralised collagen fibrils were aligned perpendicular to the long axis of the DCB sample. A representative image of the area around the start of the crack (Figure 7b) shows the fibrils were organised perpendicular to the crack path and were well organised. In

the region of tissue adjacent to the broken shoulder of DCB (Figure 7c) and below the straight crack, the crack path was aligned perpendicular to the fibrils. The SAED pattern (Figure 7d) from this region (denoted by asterisk) presented a (002) arc characteristic of hydroxyapatite and confirms that the mineralised fibrils were aligned normal to the straight crack direction.

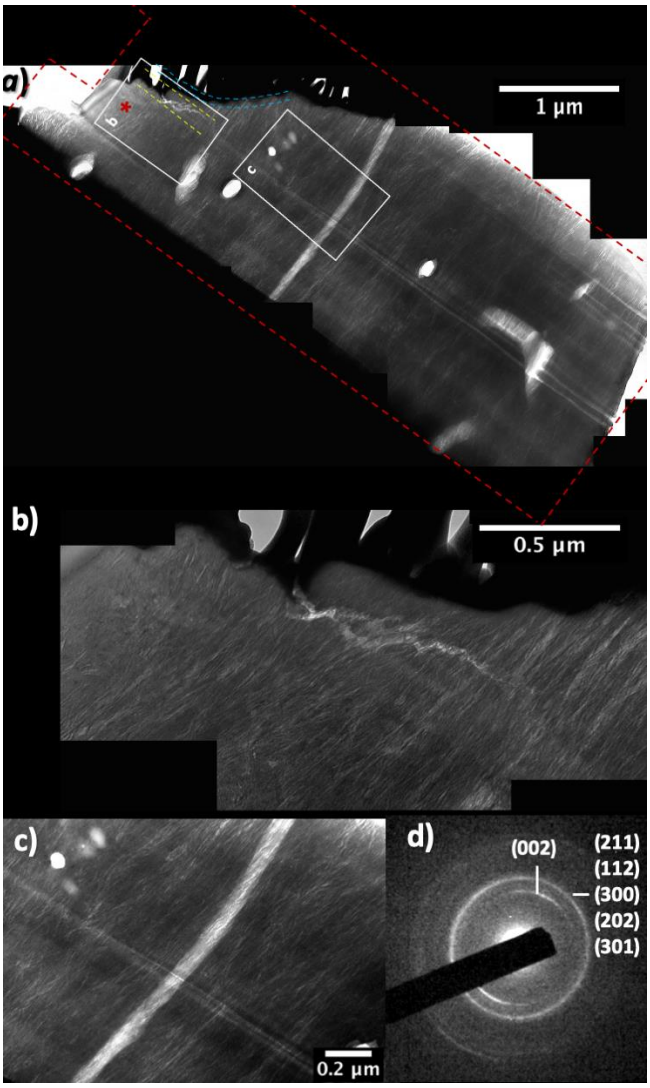

Figure 7. TEM images of the fractured DCB from the pillar in Figure 4d (OPN3). **(a)** A short straight crack (delineated by two yellow dotted lines) and an abruptly deflected crack (delineated by two blue dotted lines) that broke the right shoulder leaving the slanted right edge; the red dotted line outlines the original DCB shape. **(b)** In the area around the short crack and adjacent to the deviated crack [white boxed region b in (a)] the mineralised fibrils were aligned perpendicular to the DCB's long axis. **(c)** In the region of the tissue next to the broken shoulder of the DCB [white boxed region c in (a)], the mineralized collagen fibrils are organized and aligned perpendicular to the long axis of the DCB. The white line in the middle of the image is a result of the FIB milling process. **(d)** A SAED pattern indexed to crystalline hydroxyapatite from the area indicated by an asterisk in (a); the characteristic arc of (002) reflection indicates that the c-axes of the mineral crystals were aligned perpendicular to the long axis of bone, and transverse to the long axis of the DCB pillar.

4. Conclusion

Nanoindentation reported values of the longitudinal elastic modulus of OPN-deficient bone were 20–35 GPa [23,24]. Similar to previous micropillar elastic modulus measures of dry *ovine* bone [17] and our previous measures of dry WT mouse [6], the OPN-deficient bone had marked anisotropic material properties likely due to the orientation of the mineralized collagen fibrils.

In the transverse direction, the stress-strain curve exhibited a nearly linear elastic regime until failure, indicating brittle behavior. A considerable plastic region was displayed by the longitudinal micropillars, indicating a quasi-brittle behaviour. A possible rationale for brittle behavior in the transverse direction may be the deformation mechanisms at the nanoscale, where alteration to the collagen fibrils structure suppresses inter-fibrillar sliding. That is, due to patchy disorganization within $OPN^{-/-}$ tissue, the average number of organized collagen fibrils spanning the transversal micropillar reduces considerably. This is likely reflected in a decrease in the number of collagen fibrils available to take part in inter-fibrillar sliding events, and thus markedly repressing the amount of plasticity.

The local microstructure of bone is naturally heterogeneous (in parameters such as lacunae, canaliculi, fibrils organization, degree of mineralization, *etc.*), and properties vary based on the region selected for fabricating the micropillars. Even so, the probability of pre-existing pores and other large structural features were minimized with the micropillar size, as traces were not detected in the pre-deformed micropillars. Yet, imaging alone does not eliminate the possibility of the occurrence of such structural features inside the micropillar. Thus, slight deviations in the measured results were expected. In fact, the presence of pre-existing features, such as lacunae and canaliculi within the micropillar would be considerable in size in comparison to the micropillar itself. The diameter of lacunae ranges from 0.05 to 0.41 μm and canaliculi diameter ranges from 0.08 to 0.71 μm [25]. A previous study [26] has indicated that the elastic modulus has a roughly cubic relationship with the volume fraction of compact bone. In the same manner, a previous experimental analysis of porous hydroxyapatite ceramic has revealed that the compressive strength correlates linearly with porosity volume [27]; a smaller pore fraction associates with a higher compressive strength. Thus, the longitudinal uniaxial ultimate stress of micropillars is approximately 3.5 times higher than that obtained macroscopically (~0.3 GPa) [17].

For $OPN^{-/-}$ tissue, the DCBs' micromechanical response either: 1) Propagated a single crack for a short length (~3 μm) before diverting in an oblique path or 2) Fractured with both a vertical crack (~0.5–2 μm) and another abruptly deflected crack. Although the TEM sample was somewhat distorted, it appeared that, when the crack encountered an organised arrangement of fibrils perpendicular to its growth direction, it deflected. Regions of disorganised fibril structure facilitated extension of the crack without deflection, as predicted for isotropic materials. This observed heterogeneity in the organisation of the tissue is characteristic of $OPN^{-/-}$ tissue [7]. We have shown previously, using electron microscopy nanodiffraction [7], that $OPN^{-/-}$ has a broader distribution of mineral orientations that WT bone. Hydrated whole bone three point bending measurement found reduced toughness in

$OPN^{-/-}$ (3.9 MPa$\sqrt{m}$) compared to WT bone (5.6 MPa$\sqrt{m}$) [8]. Conventional microindentation tests (with an indentation size of ~ 50 µm) [28] of mouse bone lacking OPN, also showed a small difference between the fracture toughness of WT and OPN deficient bone (~ 4.3 MPa$\sqrt{m}$ for OPN deficient *vs.* ~ 5.8 MPa$\sqrt{m}$ for WT bone). In this work, we measured a transverse fracture toughness of $OPN^{-/-}$ of 0.06 MPa$\sqrt{m}$ (G =0.9 J/m^2), and in our previous studies we estimated a fracture toughness in transverse WT DCB samples tested dry to be around 0.7 MPa$\sqrt{m}$ (fracture energy G = 26 J/m^2 [6]). Interestingly, this value of fracture toughness for OPN-/- bone is similar to the fracture/surface energy for hydroxyapatite [29], which suggests a limited contribution from the collagen/mineral phase. This highlights three interesting features: 1) The fracture toughness tested at small length scales (micro-toughness) is significantly less than bulk toughness at the whole bone level; 2) $OPN^{-/-}$ fracture toughness is significantly less than WT toughness; 3) the difference between WT and $OPN^{-/-}$ is greater at the smaller length scales.

Bulk vs. micro-toughness: Previous investigations of bone at the macroscopic scale have clearly shown that hydration increases the work of fracture [30–34]. In addition, R-curve measurements indicate that the fracture toughness of dry and hydrated bone raises to values far greater than the dry micro-toughness as the crack lengths grow up to hundreds or thousands of microns. This is due to the presence of additional structural features at larger length scales that contribute to fracture resistance. Work of fracture characterizes the resistance of bone to total crack propagation process [21]. Indeed, water is crucial through imparting ductility to the collagen matrix [35], increasing collagen packing [36] and eventually influencing the collagen–mineral interactions [37]. Our measurements of fracture energy assess resistance to crack initiation, where the role of water remains unclear. Although hydration has been shown to increase significantly the macroscopic work of fracture, it is not established if it leads to an increase in crack initiation toughness [31,32] (or decrease for that matter [38]). However, the reduced fracture energy in the current study compared to wet or dry bulk toughness measurements of OPN-deficient bone can be explained because we are probing fracture properties at length scales smaller than the length scale of many extrinsic toughening features (porosity and osteons). Although our findings are drawn from dry bone, it offers a baseline to systematically expand and advance the understanding of water's role on bone's fracture behavior on a few micrometers scale.

$OPN^{-/-}$ vs. WT: In our previous study on WT bones, we were not able to obtain fracture toughness values directly from experiments on bone in the transverse direction because the crack deflected immediately [6]. Our phase field models indicated that as anisotropy increases, the deflection increases. In $OPN^{-/-}$ bone, for the transverse direction, we were able to obtain at least a short straight crack before deflection, indicating that anisotropy is likely smaller than in WT bones. In all four samples, local anisotropy had a strong effect on the fracture path. In samples with disorganized collagen at the top of the pillar (OPN1 and OPN2, Figure 3b), the crack proceeded straight as predicted from linear elastic fracture mechanics for isotropic materials. and orthotropic materials along the fiber direction (such as the longitudinal direction of WT bones). When the crack came to an organized region of collagen, with the fibrils perpendicular to the crack direction, the crack was deflected. In

samples that had perpendicularly organized collagen at the top of the pillar (OPN 3 and OPN4, Figure 4), the crack was immediately deflected. Therefore, poor collagen organization may contribute towards the decrease in transverse fracture toughness of OPN bone compared to WT which is also reflected by the variation in fracture energy values between OPN1/2 and OPN3/4. Many studies have shown the importance of fibril orientation on fracture properties in micro 3- and 4-point bending of trabecular lamellae [39], micro-tension of lamellar bone [40], and compact-tension samples of dentin [41]. Another important contributory parameter to consider is the role that OPN plays as a glue that holds the collagen fibrils together [42]. Energy is dissipated when the glue is stretched, through rupturing of "sacrificial bonds"-weak, reformable bonds that break before the strong covalent bonds that hold the molecules together—contributing to toughening. Therefore the OPN deficiency may reduce energy dissipation at this scale *via* this combination of mechanisms involving both altered collagen organization and its role in "glueing" the collagen fibrils together. In our previous work we also measured a significant reduction in mineral density in OPN-/- tissue compared to WT tissues suggesting that changes in mineral density could also contribute [7].

$OPN^{-/-}$ vs. WT at different length scales: Whole bone fracture toughness of $OPN^{-/-}$ was about 30% lower than WT in the transverse direction [8]; while here it is shown that at the micro-scale fracture toughness of $OPN^{-/-}$ was an order of magnitude less that WT. This could be due to effects of anisotropy being more pronounced at small length scales because of the lack of other toughening mechanisms. This is supported by the strong dependence of crack path on fibril organization at the micro-level which is shown here.

The analysis suggests that the skeletal phenotype of OPN-/- mice disrupts the ultrastructural structure of the bone matrix in localized regions, which reduce fracture resistance. Although healthy bone resists fracture propagation through a pronounced anisotropic behavior [6,43], OPN-deficient bone exhibits less consistent cracking behavior. This apparent observation seems to originate from the interplay between the less organised bone matrix and toughening mechanisms acting at the small-length scales. These findings further support the general notion that OPN deficient tissue displays variability in the packing degree of fibrils [36–38]; which may contribute to the tissue's varied capacity for intrinsic plasticity mechanisms that promote ductility.

The average measured fracture energy for OPN-mutant mouse bone, in the transverse direction, at the microscale was 0.94 ± 0.67 J/m^2, which is significantly lower than wild type bone, which was estimated to be around 26 J/m^2 [6]. TEM images illustrate that the diminished fracture toughness of OPN deficient bone could be explained, in part, by its patchy, heterogeneous organization at the fibrillar level. The cracks were able to propagate through regions of poorly organized tissue, whereas they were deflected in regions of well-organized tissue. This micromechanical investigation would benefit from a higher number of samples tested using DCB micropillars. This was not conducted due to the considerable time and effort required for fabricating micropillars with FIB. However, the quantified response of microscale fracture resistance accompanied by the influence of the fibrillary structure serves as a baseline to explore further the correlation between the ultrastructure, organisation and

fracture resistance at small-length scales. Such insight can potentially lead to design of more efficient biomimetic materials.

Supplementary data

The authors confirm that the supplementary data are available within this article.

Acknowledgment

Funding: The authors would like to acknowledge funding by King Saud bin Abdulaziz University for Health Sciences to N.A. and Wellcome Trust grant: WT097347AIA to A.E.P. and S.S. and Shell Research. We would like to thank Giorgio Sernicola for help with the mechanical testing.

Conflicts of interests

All authors declare they have no competing financial interests.

Ethical statement

The study was approved by the Northeastern Institutional Animal Care and Use Committee (May 8 2017, #17-0515R).

Authors' contribution

Conceptualization, N.A., F.G., A.E.P., S.J.S. and E.S.; methodology, N.A., F.G., A.E.P., S.J.S. and E.S.; formal analysis, N.A; investigation, N.A.; resources, F.G., A.E.P., S.J.S. and X.X.; writing—original draft preparation, N.A., F.G., A.E.P., S.J.S. and E.S.; writing—review and editing, N.A., F.G., A.E.P., S.J.S. and E.S.; supervision, F.G., A.E.P., and S.J.S.; funding acquisition, F.G., A.E.P., and S.J.S. All authors have read and agreed to the published version of the manuscript.

References

[1] Riggs BL, Melton LJ. Involutional osteoporosis. *N. Engl. J. Med.* 1986, 314(26):1676–1686.
[2] Kanis JA. Diagnosis of osteoporosis and assessment of fracture risk. *Lancet.* 2002, 359(9321):1929–1936.
[3] Schuit SC, van der Klift M, Weel AE, de Laet CE, Burger H, *et al*. Fracture incidence and association with bone mineral density in elderly men and women: the Rotterdam Study. *Bone*. 2004, 34(1):195–202.
[4] Ott SM. When bone mass fails to predict bone failure. *Calcif. tiss. int.* 1993, 53(1): S7–S13.
[5] Launey ME, Buehler MJ, Ritchie RO. On the Mechanistic Origins of Toughness in Bone. *Annu. Rev. Mater. Res.* 2010, 40:25–53.
[6] Aldegaither N, Sernicola G, Mesgarnejad A, Karma A, Balint D, *et al*. Fracture toughness of bone at the microscale. *Acta Biomater.* 2020, 121:475–483.

[7] Depalle B, McGilvery CM, Nobakhti S, Aldegaither N, Shefelbine SJ, *et al*. Mapping the Effect of Osteopontin on Collagen Structure and Mineralization at the Nanoscale. *Acta Biomater*. 2020, 120:194–202.
[8] Thurner PJ, Chen CG, Ionova-Martin S, Sun L, Harman A, *et al*. Osteopontin deficiency increases bone fragility but preserves bone mass. *Bone.* 2010, 46(6):1564–1573.
[9] Duvall CL, Taylor WR, Weiss D, Wojtowicz AM, Guldberg RE. Impaired angiogenesis, early callus formation, and late stage remodeling in fracture healing of osteopontin-deficient mice. *J. Bone Miner. Res.* 2007, 22(2):286–297.
[10] Nikel O, Poundarik AA, Bailey S, Vashishth D, Structural role of osteocalcin and osteopontin in energy dissipation in bone. *J. Biomech.* 2018, 80: 45–52.
[11] Kavukcuoglu NB, Denhardt DT, Guzelsu N, Mann AB. Osteopontin deficiency and aging on nanomechanics of mouse bone. *J. Biomed. Mater. Res*. 2007, 83(1):136–144.
[12] Fei H, Abraham A, Chawla N, Jiang H. Evaluation of micro-pillar compression tests for accurate determination of elastic-plastic constitutive relations. *J. Appl. Mech.* 2012, 79:061011.
[13] Zhang H, Schuster BE, Wei Q, Ramesh KT. The design of accurate micro-compression experiments. *Scr. Mater.* 2006, 54(2):181–186.
[14] Sandoval D, Rinaldi A, Tarragó JM, Roa JJ, Fair J, *et al.* Scale effect in mechanical characterization of WC-Co composites. *Int. J. Refract. Met. Hard Mater.* 2018, 72:157–162.
[15] Sernicola G, Giovannini T, Patel P, Kermode JR, Balint DS, *et al*. In situ stable crack growth at the micron scale. *Nat Commun*. 2017,8(1):108.
[16] Zhang H, Schuster BE, Wei Q, Ramesh KT. The design of accurate micro-compression experiments. *Scripta Materialia*. 2006, 54(2):181–186.
[17] Schwiedrzik J, Raghavan R, Burki A, LeNader V, Wolfram U, *et al*. In situ micropillar compression reveals superior strength and ductility but an absence of damage in lamellar bone. *Nat. Mater.* 2014, 13(7):740–747.
[18] Timoshenko SP, Gere JM. Theory of elastic stability. *McGraw-Hill*. 1961.
[19] Shahar R, Zaslansky P, Barak M, Friesem AA, Currey JD, *et al.* Anisotropic Poisson's ratio and compression modulus of cortical bone determined by speckle interferometry. *J. Biomech.* 2007, 40(2):252–264.
[20] Williams JG. End corrections for orthotropic DCB specimens. *Composit. Sci. Tech.* 1989, 35(4):367–376.
[21] Anderson TL. *Fracture mechanics: fundamentals and applications*. 4th ed. St Boca Raton: Taylor & Francis, 2017.
[22] Sih GC, Paris PC, Irwin GR. On cracks in rectilinearly anisotropic bodies. *Int. J. Fract. Mech.* 1965, 1:189–203.
[23] Thurner PJ, Chen CG, Ionova-Martin S, Sun L, Harman A, *et al*. Osteopontin deficiency increases bone fragility but preserves bone mass. *Bone.* 2010, 46(6):1564–1573.
[24] Kavukcuoglu NB, Denhardt DT, Guzelsu N, Mann AB. Osteopontin deficiency and aging on nanomechanics of mouse bone. *J. Biomed. Mater. Res. A.* 2007, 83 (1):136–144.
[25] You LD, Weinbaum S, Cowin SC, Schaffler MB. Ultrastructure of the osteocyte process and its pericellular matrix. *Anat. Rec. A. Discov. Mol. Cell Evol. Biol.* 2004, 278 (2):505–513.
[26] Currey JD. The effect of porosity and mineral content on the Young's modulus of elasticity of compact bone. *J. Biomech.* 1988, 21(2):131–139.
[27] Liu DM. Influence of porosity and pore size on the compressive strength of porous hydroxyapatite ceramic. *Ceram. Int.* 1997, 23(2):135–139.
[28] Poundarik AA, Diab T, Sroga GE, Ural A, Boskey AL, *et al.* Dilatational band formation in bone. *Proc. Natl. Acad. Sci*. 2012, 109(47):19178–19183.
[29] Zhu W, Wu P. Surface energetics of hydroxyapatite: a DFT study. *Chem. Phys. Lett.* 2004, 396(1–3):38–42.

[30] Adharapurapu RR, Jiang F, Vecchio KS. Dynamic fracture of bovine bone. *Mater. Sci. Eng. C.* 2006, 26(8):1325–1332.
[31] Lucksanasombool P, Higgs WAJ, Higgs RJED, Swain MV. Fracture toughness of bovine bone: influence of orientation and storage media. *Biomaterials.* 2001, 22(23):3127–3132.
[32] Nalla RK, Balooch M, Ager Iii JW, Kruzic JJ, Kinney JH, *et al.* Effects of polar solvents on the fracture resistance of dentin: role of water hydration. *Acta Biomater.* 2005, 1(1):31–43.
[33] Smith NW, Ekwaro-Osire S, Khandaker M, Hashemi J. Influence of storage duration on retention of original fracture toughness. *Exp. Mech.* 2011, 51:697–705.
[34] Yan J, Daga A, Kumar R, Mecholsky JJ. Fracture toughness and work of fracture of hydrated, dehydrated, and ashed bovine bone. *J. Biomech.* 2008, 41(9):1929–1936.
[35] Yamashita J, Li X, Furman BR, Rawls HR, Wang X, *et al.* Collagen and bone viscoelasticity: a dynamic mechanical analysis. *J. Biomed. Mater. Res.* 2002, 63(1):31–36.
[36] Lees S. A mixed packing model for bone collagen. *Calcif. Tissue Int.* 1981, 33:591–602.
[37] Bonar LC, Lees S, Mook HA. Neutron diffraction studies of collagen in fully mineralized bone. *J. Mol. Biol.* 1985, 181(2):265–270.
[38] Granke M, Does MD, Nyman JS. The Role of Water Compartments in the Material Properties of Cortical Bone. *Calcif. Tissue Int.* 2015, 97:292–307.
[39] Tertuliano OA, Edwards BW, Meza LR, Deshpande VS, Greerr JR. Nanofibril-mediated fracture resistance of bone. *Bioinspir. Biomim*. 2021, 16(3):035001.
[40] Casari D, Kochetkova T, Michler J, Zysset P, Schwiedrzik J. Microtensile failure mechanisms in lamellar bone: Influence of fibrillar orientation, specimen size and hydration. *Acta Biomater*. 2021, 131:391–402.
[41] Nalla R, Kinney JH, Ritchie RO. Effect of orientation on the *in vitro* fracture toughness of dentin: the role of toughening mechanisms. *Biomaterials.* 2023, 24(22):3955–3968.
[42] Fantner GE, Hassenkam T, Kindt JH, Weaver JC, Birkedal H, *et al.* Sacrificial bonds and hidden length dissipate energy as mineralized fibrils separate during bone fracture. *Nat. Mater.* 2005, 4(8):612–616.
[43] Casanova M, Balmelli A, Carnelli D, Courty D, Schneider P, *et al*. Nanoindentation analysis of the micromechanical anisotropy in mouse cortical bone, *R. Soc. Open Sci.* 2017, 4(2):160971.